Cal Maritime Collegiate Wind Technical Design Report 2023

Prepared for the United States Department of Energy Collegiate Wind Competition

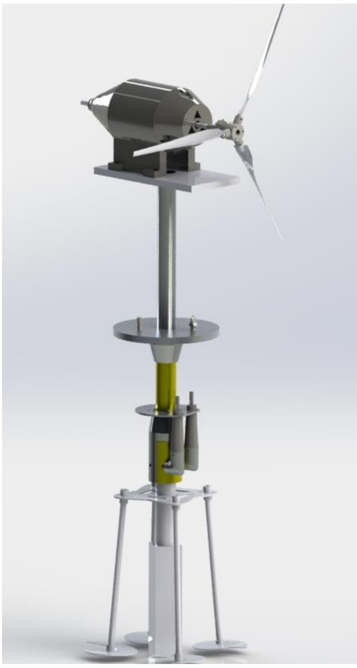

Jake Nelson	Turbine Design Manager & Blades Lead
Sidharth Kumar	Team Coordinator & Electronics/Controls Lead
Matthew Thomas	Foundation Lead
Anthony Butler	Generator Lead, Tower/ Nacelle Lead
Lucian Drogo	Mechanical Pitch Lead
Miles Krauter	Foundation, Electronics/Controls
Evan Fishel	Generator Lead, Connection Creation Lead
Faculty Advisors:	Dr. Thomas Nordenholz
	Professor Michael Strange
	Professor Steffan Long
	Dr. Zachary Nosker
	Professor David Grover

Submitted May 4th, 2023, for the US Department of Energy's Collegiate Wind Competition

California State University Maritime Academy

200 Maritime Academy Dr, Vallejo CA, 94590

Sponsor

Hornblower Bridgeport, CT Shipyard™

Table of Contents

Chapter 1: Executive Summary

Our turbine design is characterized as a three-blade horizontal axis rotor, with a variable pitching mechanism that transfers torque into the shaft and allows for change in pitch angle. We convert the mechanical energy into electrical energy through a custom-built, three phase generator that is rectified from AC power to DC power across a variable resistive load. The entire turbine is anchored by a fixed-bottom foundation, which is comprised of four helical screw discs anchored into the sand, and a hollow box section in the center for additional stability.

The purpose of the turbine design is to achieve the following tasks in an effective manner: maximize power at low wind speeds below 11m/s, control turbine power and speed for wind speeds above 11m/s, and safely shutdown and restart our turbine for emergency stop and load disconnect conditions all while maintaining durability for all operating states.

To maximize power, we used a blended airfoil design for the blades with airfoils that are aggressively thinner relative to previous years for efficient aerodynamics, we designed an in-house generator to eliminate cogging torque and customize our operating voltage, and we designed a variable resistive load to vary the speed to the turbine's maximum power point during the power curve task.

At wind speeds above 11m/s, we control the turbine's power and speed by varying the pitching angle of the rotor to maintain rated power and speed. This year, we redesigned the pitching mechanism as a novel rotary miter gear design to increase reliability. Serial communications between the turbine and load electronic controllers will be in place to shut the turbine down, and restart with ease – capacitors across the bus voltage on the turbine electronics will store the minimum power required for operation of our pitch mechanism and controller to complete the shutdown, and a latching relay will be in place to electrically short the turbine for redundancy.

Finally, we properly sized our components for durability based on our states of operation. Our components under scrutiny will be those that are under load and 3D printed. These components were printed using natural PLA, with a tensile strength of 59MPa[1]. The first state is maximum power at 11m/s, where the rotor begins to pitch into the wind. We expect there to be a local maximum of thrust and will consider that in our foundation design analysis. The second state is pre-cut out wind speed at rated rotor speed, or 14m/s and 3000RPM. This will only affect the durability of the blades as they will be subject to extreme bending moments and moderate centrifugal forces. The third state is the runaway rotor, which we predict will take place at 12m/s and an extreme rotor speed of 4500 RPM. The shaft speed was chosen based on experimentally disconnecting the load, and the wind speed was predicted based on data from previous competitions. The generator, blades, and pitch mechanism will be under consideration with the excess centrifugal forces in mind. Finally, we have the fourth state where the turbine is parked at 0 RPM, 22m/s, where the foundation will be subject to maximum aerodynamic drag.

All analysis and testing was done at sea level, with an air density of $1.225\frac{kg}{m^3}$. We expect a decrease in power and thrust loads proportional to the decrease in air density at Colorado's higher elevations.

Chapter 2: Blades

2.1 Initial Airfoil Selection

The first step in the design process is selecting the airfoils for efficient and reliable power extraction at our scale. We use a blended airfoil design for power production along the span of the blade and structural integrity near the root to withstand high bending moments. Because of our 45cm diameter rotor constraint, it was assumed that we would be subject to a low Reynolds number flow regime, so we picked our airfoils with that in mind. Furthermore, prior team reports have opted towards using airfoils with thickness-to-chord ratios (t/c) of greater than 9%, even though thinner airfoils tend to be more efficient. We picked the CR001SM airfoil, with t/c of 7.1%, to occupy 90% of the blade span to the tip for its higher lift/drag ratio (C_L/D_D) of 41.2, compared to our benchmark of 40.08 from one of our winning teams, the 2020 Maritime team[2]. Furthermore, the GOE 623 was selected for its t/c of 12%, along with having a similar peak C_L/D_D angle of attack and geometric properties.

2.2 Blade Design

2.2.1 Optimized Blade Geometry

Our blade geometry is designed for maximizing power along each section of its span. We use the Schmitz Optimization algorithm, which is derived from Blade Element Momentum Theory (BEM Theory), to design an optimal chord (c) & twist (θ) distribution along the blade length for a given tip speed ratio (see Figure 2.2.1). Upon designing a blade geometry, we validated our Reynolds Number using the chord length, relative wind velocity, and kinematic viscosity. Once a blade design was chosen, we imported the geometry into QBlade, an open-source blade design and aerodynamic simulation software developed by the TU Berlin, to simulate our design. Qblade uses BEM Theory to compute the torques and forces on the rotor to analyze power output and loads.

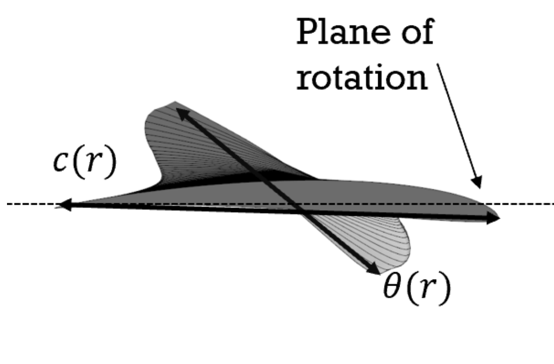

Figure 2.2.1: Blade Geometry Design

2.2.2 Cp vs. TSR Curves

A key result of BEM theory and indicator of rotor performance, from the standpoint of power production and controllability, is its non-dimensional power vs. rotor speed curve, or C_P vs. TSR curve. Shown on Figure 2.2.2 is the power performance curve for this year's blade design. We use these curves to compare different blended airfoil designs with a Schmitz optimization geometry based on their peak C_P when the rotor is at full run and operating at peak TSR. When applying Schmitz, as discussed in 2.2.1, it is important to iterate tip speed ratios and analyze the rotor performance using these curves. Additionally, the Schmitz optimization does not account for drag losses, so varying θ is necessary

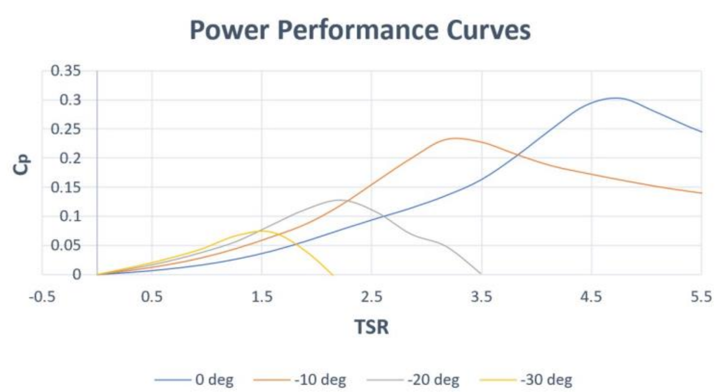

Figure 2.2.2: Power Performance Curves

to correct for drag. After our final iteration, our blade design maximizes C_P from 0.3-0.35. We also evaluated the viability of speed control based on how broad these curves are, and our blade design appears to suit that criterion based on the curves which ended up translating through our experimental data. Finally, we are looking for an appreciable decrease in C_P as the rotor pitches into the wind, which is what we observe in Figure 2.2.2. This will be the basis for how we control for rated power at high wind speeds.

2.2.3 Manufacturing

QBlade also allows us to export a 3D model into Solidworks as an STL file. This allows us to put a root connection on the end of the blade to interface with the pitch mechanism. We then manufacture the blades by slicing and 3D printing the model, shown in **Error! Reference source not found.**, out of PLA. 3D printing offers the advantage of easy and rapid prototyping that other methods do not have, which has allowed us to experiment with different aerodynamic concepts such as winglets (shown in Figure 2.2.3) for reduced tip vortices, and trips on the leading edge to delay stall and yield a higher C_L/C_D.

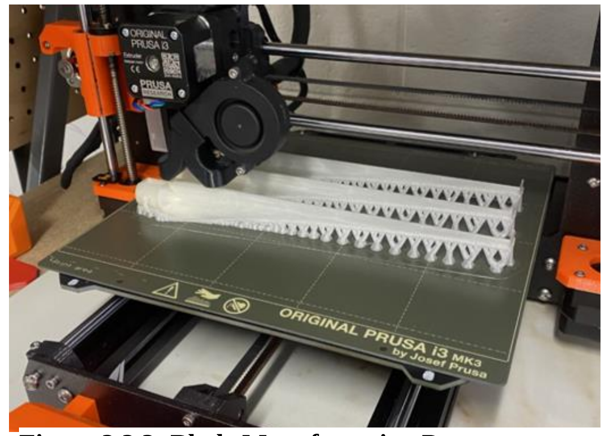

Figure 2.2.3: Blade Manufacturing Process

2.3 Mechanical Loads Analysis

2.3.1 Blade Span

Our model for the span of the blade is a rotating cantilever beam, with neglected twist and area properties approximated based on an MIT aerodynamics lecture[3]. The beam is subject to wind loading on the flapwise side, calculated by QBlade, and centrifugal loads that cause a restoring moment to the blade's deflection from the wind, also known as centrifugal stiffening. To accurately account for the loads on the blade, we accounted for the effect of centrifugal stiffening with a fourth order differential equation in terms of the centrifugal force, the wind loading, and internal forces as a function of the radius. Solving this equation required iteration of the slope profile of the blade which converges towards an accurate solution. Using this converged profile can lead to computing internal loads and, subsequently, stresses. The results for the runaway rotor state and pre-cut-out state can be found in Table I. It should also be noted that the maximum axial force is 200N, and that has relevance for our root stress analysis.

Table I: Load Analyses Results

Operating States	Stress	Deflection	FS
Runaway Rotor	2.6MPa	0.145mm	21.2
Pre Cut-Out	1.2MPa	0.236mm	45.4

2.3.2 Root Connection

Our root connection is essentially a hollow cylinder pinned to the blade mount. Shown in Figure 2.3.2 is the axial load acting on the root (the bending moment is neglected for its insignificant contribution). Only the runaway state will be considered in this analysis since that is where the axial load is the greatest. Within this analysis, there are two failure modes: the normal stress concentration along its axial plane, and tangential stresses along the planes of maximum shear. We solved for the stress concentration using Roark's Formula for Stress and Strain and

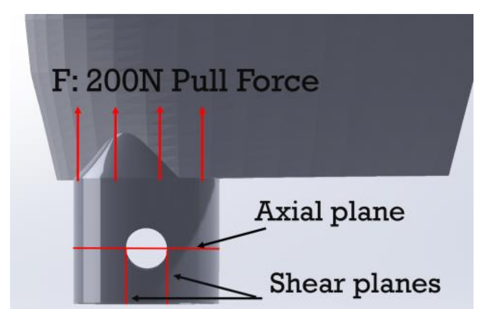

Figure 2.3.2: Root Connection Loads

solved for the stresses in both modes of failure[4]. PLA is a brittle material, so we used the Max Normal Stress failure theory as a suitable criterion for strength. We determined that the root would exhibit the highest stresses along the axial plane due to the stress concentration, with a safety factor of 4.

Our experimental blade rigidity was validated through repeated wind tunnel testing for fixed pitch power curve and runaway rotor conditions, with the blades showing no signs of excessive deformation.

Chapter 3: Mechanical Design

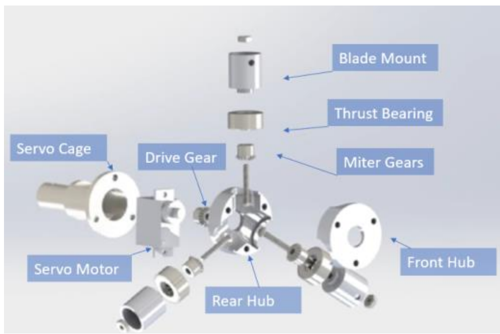

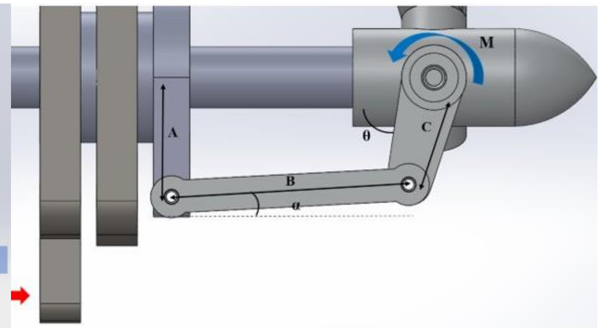

Figure 3.1: Rotary Pitch **Figure 3.2: Linear Pitch[5]**

3.1 Pitch Overview

In previous years, Cal Maritime and many other teams have used a linearly actuated pitch, pictured in Figure 3.2. The linear pitch designs use systems of linkages driven by a linear actuator. These linkages add complexity to design and manufacturing. The plate must slide along the shaft which leads to metal-on-metal friction. The rotary pitch, pictured in Figure 3.1, was chosen to limit friction and complexity while aligning more closely with the design of a commercial wind turbine. Changing the design also allowed us to learn much more than we would have by relying on the basics from already established designs. This year’s pitch allowed us to learn about slip rings and brushes, and the proper mounting and meshing of gears, along with other lessons that come with a new design.

3.2 Pitch Assembly

The pitch this year consists of a servo motor and 4 miter gears to control the blades. The components are pictured in Figure 3.3. The servo cage holds the servo in place and is affixed to the shaft using set screws. Slip rings are also on the shaft to transmit power from electrical brushes. The servo’s drive gear meshes with the other three miter gears and turns them in unison. The miter gears are bolted to the blade mounts. The blades are bolted in place on the blade mounts. The thrust bearing transmits the centrifugal forces on the blades to the gearbox. This bearing has a smooth rotating inner run which the bearing gear can press against while still rotating freely. The gear box holds the gear and blade assemblies together. In Figure 3.3, one of the 3-blade gear assemblies is constructed to show a clear view of the gears meshing and how the blade attaches.

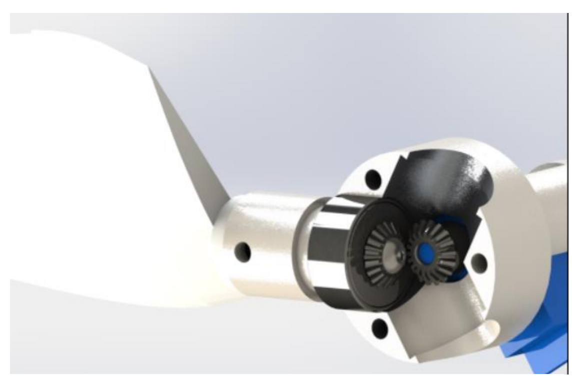

Figure 3.3 Partially Assembled Pitch

3.3 Stress Calculations

The wind forces on the blades result in load being transferred to the pitch. The centrifugal force on the pitch was calculated to be 200 Newtons. The weakest point for this load is on the walls of the hub where the thrust bearing sits. Using SolidWorks FE Analysis, pictured in Figure 3.4, the highest principal stress was found to be about 25 MPa, which has a factor of safety of about 2. Max Normal Stress theory was calculated to predict the failure of the blade mount. The weakest point is the pinhole that connects the blade mount to the blade root. The maximum shear stress is about 7 MPa which gives the system a factor of safety of about 8.4. The largest pitching moment was found to be 0.011 Nm while in the runaway state of the turbine. In this state, there is no load on the generator and the wind is at 12m/s. The servo motor was sized to handle 0.196 Nm.

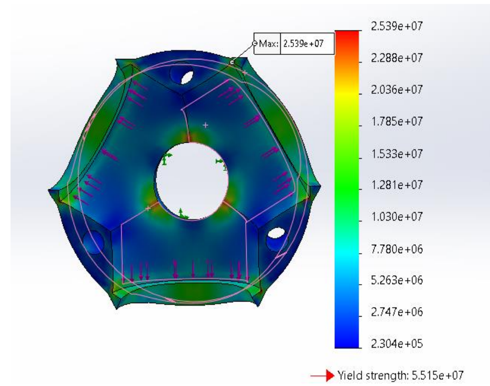

Figure 3.4 FEA Front Hub

3.4 Results

The pitch showed potential when it was tested. It has a quick response time, and precise controllability at low wind speeds. At higher wind speeds, it is having trouble feathering to slow its rotation. This problem can be mitigated by increasing the load or stalling the blades enough to allow for the rpm to decrease, leading to conditions under which the blades can feather. The pitch's poor performance is likely due to improper gear meshing. Recently, sleeve bearings have been added to the gear blade assembly to mitigate this problem. These bearings run along the gear box to support against transverse loads as it was found that the thrust bearing does not do this. This improvement will keep the angle of gear meshing consistent. As a result of 3D printing, some of the dimensions vary from what they were designed to be; this has led to the distance between the gears to be incorrect. To account for this, the position of the drive gear has been made adjustable to tweak the gear meshing.

Aside from the poor torque performance, the pitch design has been successful. The drive gear was successfully affixed to the servo motor and the blades and gears stay aligned after extended use, enabling continued precise control. The gearbox and servo cage showed no signs of wear or deformation. The gearbox could be redesigned to print more precisely, which would enable better gear meshing. There was concern that the brushes would cause significant friction to the shaft, leading to dramatically lower power output. With some adjustment to the brush springs, the friction has been reduced to have no significant effect on power output.

Overall, the pitch system needs some adjustments. These adjustments will hopefully be done before the competition. With the design of the pitch being started from scratch, there was expectations that there would be some unresolved issues. If future teams wish to continue with this pitch design, it will be given the time it needs to be revised.

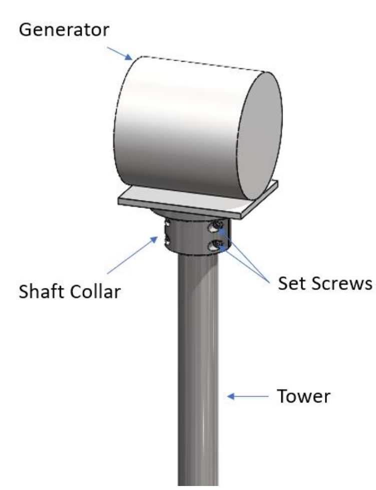

Figure 3.5 Nacelle to Tower Connection

3.5 Tower & Yaw

The team chose to go with an aluminum tower for this year. Aluminum was chosen as it is lightweight and it can be easily machined to ensure proper interfacing with other components. To connect the tower with the nacelle, a prefabricated shaft collar will be utilized. This is a divergence from previous years, which incorporated a passive yaw system. The shaft collar provides the ability to adjust the generator, and thus rotor, to be perpendicular to the prevailing wind direction. The generator can then pinned in place by tightening the attached set screws against the tower. A mock up of this arrangement is shown in Figure 3.5.

Chapter 4: Generator Design

4.1 Overview

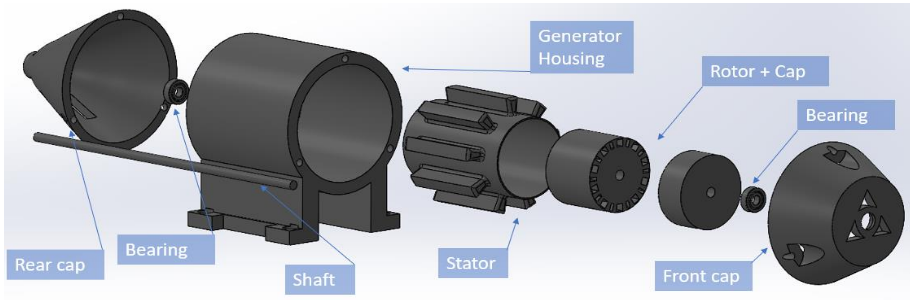

Figure 4.1 Generator Overview

Over the past several years, the teams at California Maritime have explored the possibilities of purchasing ready-made generators or constructing custom ones. After weighing the pros and cons of each option, a custom-built generator would be the most beneficial. While a commercially available generator might save time, it doesn't allow for the design flexibility needed to optimize power production at low wind speeds and mitigate the effects of cogging torque. Cogging torque, a phenomenon caused by the interaction of the magnetic field between the stator and rotor, can make the rotor resist spinning, especially at lower speeds. A custom-built generator can address these issues, potentially reducing power loss and enhancing performance at lower wind speeds. Furthermore, creating a custom generator allows for the optimization of the power curve, tailored specifically to the demands of the competition. Over the past few years, the radial flux design has proven to have effective performance in comparison to the axial design. We have agreed as a team to opt for the radial design for its reliability and simple manufacturing.

$$\mathrm{EMF} = -\frac{d\Phi}{dt}$$

Equation 4.1.1

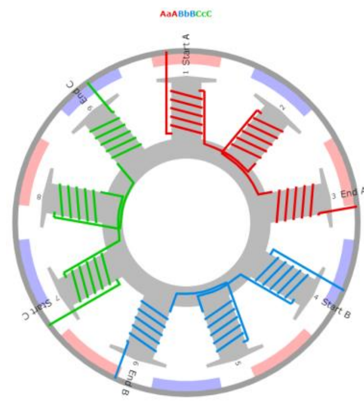
Figure 4.2 Winding Schematic[6]

4.2 Coil and Magnet Configurations

One of the main components to designing a custom-built generator is finding the characteristics of how much voltage it can produce. Faraday’s law describes how the magnetic field induces the electromotive force in a conductor, shown in Equation 4.2.1. Faraday's law can be applied to define the DC voltage output generated by our nine-coil, ten-pole generator.

The driving factor for this year's design is to facilitate rapid prototyping and experimentation with various magnet arrangements. The stator and rotor were designed to easily swap out different configurations, aiding our final decision process in finding the most effective configuration. The rotor has been designed to accommodate magnets without the need for any adhesives. The only time limiting factors were the 3D printing process and the insulated copper coil wrapping process. Multiple stators and rotors were produced using these processes. Figure 4.2 illustrates the winding configuration, with the coils being arranged in a delta connection. There were two different magnet configurations that were considered for this year's

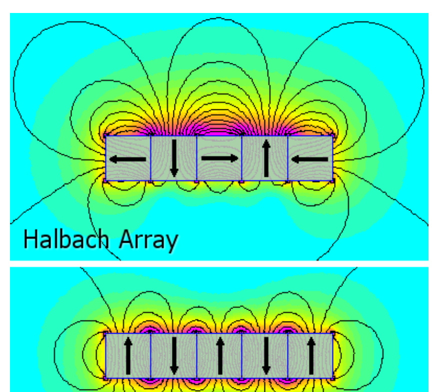

Figure 4.3: Magnet Configurations[6]

design. These were the alternating pole arrangement and the Halbach arrangement depicted in Figure 4.3. The Halbach array provides a larger magnetic field compared to the alternating polarity array. This makes up for the weakened magnetic field caused by the gap between the magnet and the coil in our encased rotor. While each array has its own benefits, this year's design will be based on the Halbach array.

$$VDC = \frac{3 * \sqrt{3} * 12NA\omega k_w B_{max}}{\pi}$$

Equation 4.2.1

In Equation 4.2.2, N represents the number of turns per coil, ω signifies our angular velocity in rad/s, B_{max} is the maximum detected magnetic field on the rotor's surface, A is the cross-sectional area of our coils, and k_w denotes the winding factor. This equation, derived from Faraday's law, was used to determine the number of coils in our current design of the generator since the output voltage is capped at 48 VDC.

4.3 Rotor Durability

The rotor, a key component of the generator, is in constant rotation within the generator's casing, supplying alternating current to the system. In the design process, an encased rotor was one of the concepts developed. This design does not necessitate the use of any adhesives to secure the magnets. Given that the rotor will be subjected to various wind speeds, the centrifugal load exerted on the PLA rotor—which serves to encase the magnets and prevent their outward displacement—must be considered. We will employ the first principle stress theory to predict whether the part will succumb to failure or withstand the centrifugal load as represented in Figure 4.4. In a comparison of the rotor's tensile strength and maximum stress, the overall safety factor was found to be approximately 3.2.

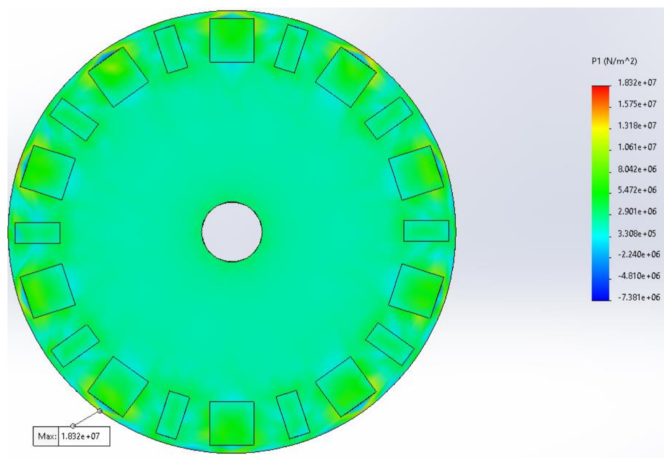

Figure 4.4: Rotor FE Analysis

4.4 Operating Voltage

The objective for this year's design is to limit our generator's maximum voltage to 48 VDC. Upon conducting various tests on the generator, the final design's peak voltage was observed to be around 55 VDC, exceeding our predefined limits. This necessitates a reduction in the number of coils wrapped on the stator. As illustrated in Figure 4.5, the unloaded operating voltage yields a slope of 0.0152 VDC/RPM, signifying a proportional relationship between RPM and voltage. Using this slope, we can determine the RPM range that will produce a voltage higher than the limit.

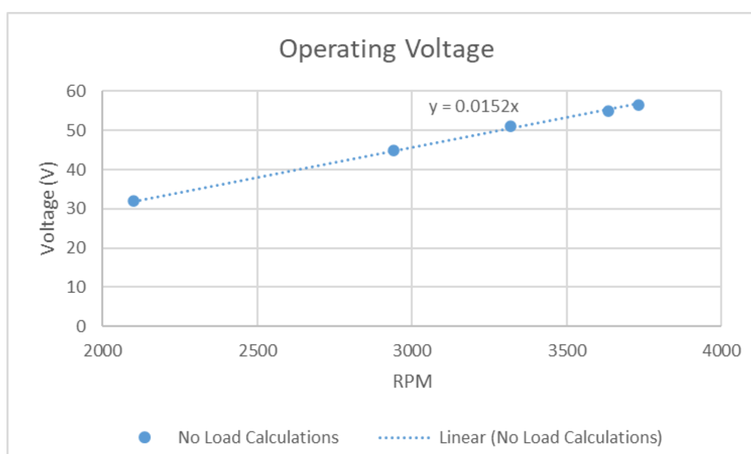

Figure 4.5 Operating Voltage

Chapter 5: Fixed-Bottom Foundation Design

5.1 Overview

This year's overall design philosophy was influenced by real world offshore wind turbine foundations, as well as the 2021-2022 Cal Maritime foundation design. We choose to keep much of the design components from the 2022 team, as their foundation was very successful at the competition. The 2022 Foundation was a hybrid fixed-bottom foundation, incorporating quad helical anchors, a monopile, and gravity elements. This year, we have chosen to retain the quad helical anchors and hybrid architecture but use alternatives to the monopile and gravity elements. This was decided with the primary goal of achieving a stable foundation, and a secondary goal of reducing the weight. A comparison between the two foundations is shown in Figure 5.1. Additionally, the design was made modular, with a bolted connection between the scribe and hollow core (Figure 5.1). This alteration assisted in the prototyping phase, when new cores were interchanged as the core design was refined.

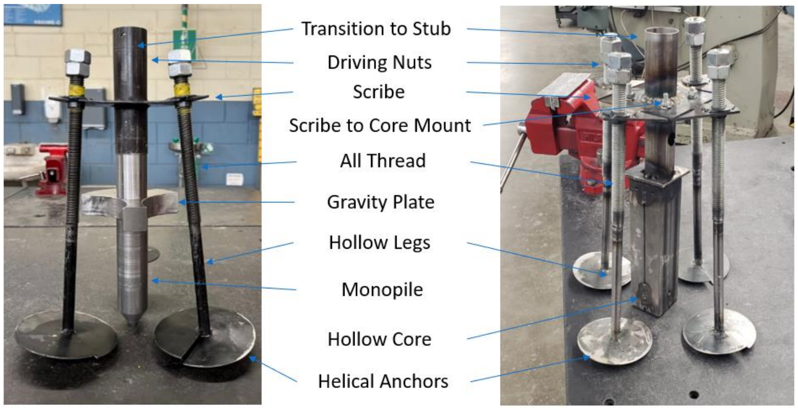

Figure 5.1 2022 vs 2023 Foundation Comparison

Taking these goals into consideration, the team looked to the industry for solutions. In this search, suction bucket technology showed promise. A suction bucket is a hollow element, typically cylindrical, that is driven into the seabed, encapsulating a trapped volume of substrate. This substrate then acts to anchor the turbine, like a gravity base, but with a center of gravity below the seabed surface. The shell acts as a monopile, imparting a force based on its contacted surface area. The key benefit of the hollow core is its low dry weight vs stability. A visual comparison of foundation styles is shown in Figure 5.2.

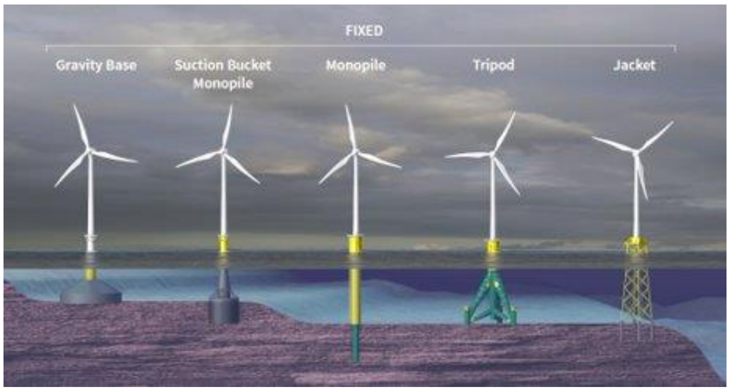

Figure 5.2 Industry Design Inspirations[7]

5.2 Foundation Integrity Analysis

To ensure the integrity of the substructure foundation system, a combination of static analysis and subcomponent testing was done to properly size the essential dimensions of our design. The primary load on the foundation is the overturning moment due to the wind loads on the turbine, which causes the anchors to fail in tension. The first step in the foundation integrity analysis was to accurately predict these loads.

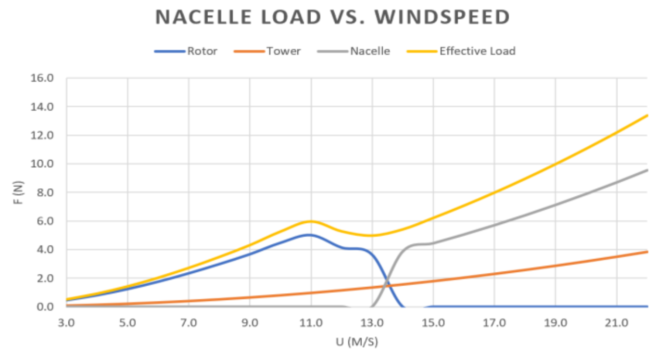

Figure 5.3: Expected Turbine Loads

5.2.1 Turbine Expected Loads

We determined that the three main loads acting on the turbine are the thrust due to the rotor, the drag on the tower, and the drag on the nacelle. We wish to determine the equivalent force at the tunnel centerline as a function of wind speed, and subsequently the maximum force. To determine the thrust on the rotor, we did a controls analysis using QBlade. This calculated the thrust as the blades begin to pitch at 11m/s to control for power, per the competition requirements. The thrust force begins to drop beyond 11m/s as the blades begin to pitch since the coefficient of thrust reduces with higher pitching angles. Both the nacelle and tower were modelled as cylinders, which is a conservative estimate, and were appropriately accounted for as such. While the nacelle's drag acts at the tunnel centerline, the tower drag acts halfway down the tower, so we determined its equivalent force contribution that acts at the nacelle. With our strategy to feather the blades to shut down for the second half of the durability task, we expect a considerable amount of thrust acting on the nacelle and for the total equivalent force at the centerline to be 14N at 22m/s (see Figure 5.3).

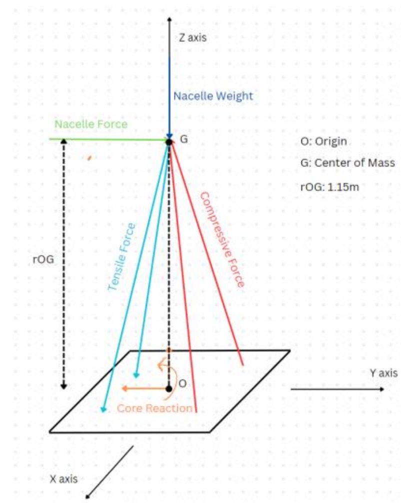

Figure 5.4: Foundation FBD

5.2.2 Foundation Free Body Diagram

Each component of turbine load induces an overturning moment on the substructure foundation. Our foundation design supports the turbine through the following as shown in Figure 5.4. Our screw anchors with diameter, D, point towards the tunnel centerline, G, of our turbine at an angle, φ, to the vertical, which is assumed to be the tunnel centerline where the equivalent nacelle force acts. Two screw anchors are in tension to pull the turbine forward and two are in compression to push the turbine forward. In addition, the hollow core provides a reaction force and moment which makes the problem statically indeterminate.

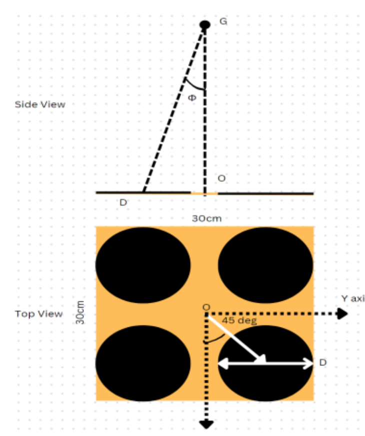

Figure 5.5: Foundation Geometry

Furthermore, changing the screw diameter affects its angle with the vertical due to the volume constraint and competition specifications as illustrated by Figure 5.5. Increasing the screw diameter means that the anchor has the capacity to take more load, but it also must take more load since it has a smaller angle with the vertical. Decreasing the diameter has the opposite effect. To move forward with this analysis, we neglected the hollow core's reaction force and calculated the forces each disc needed to exert to keep the turbine in static equilibrium. We experimentally determined how much force our hollow core design would withstand prior to failure by doing lateral pull tests, and made the problem statically determinate by adding that result in.

5.2.3 Pull Tests

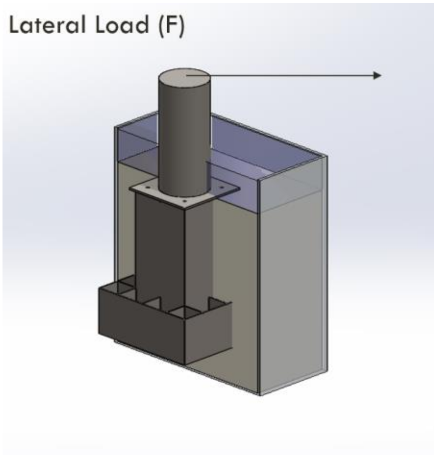

Figure 5.6: Hollow Core Test Illustration

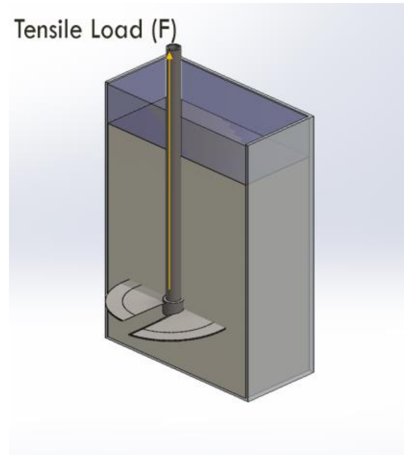

Figure 5.7: Anchor Pull Test Illustration

Performing experimental pull-tests on our two foundation components, the screw anchors, and the hollow core accomplishes three goals: it resolves the static indeterminacy introduced in our force diagram, develops a strategy to manufacture and install our two foundation components, and gives us a relationship between the screw anchor load capacity and its disk diameter. Our experimental set-up comprised of a box of sand and water with the maximum depth required by the competition and prototypes of the screw anchors and hollow core.

To test the screw anchors, we developed prototypes that varied in diameter from $2\frac{1}{2}$" to 5" in half-inch increments. For each screw anchor, we had one universal stock of all-thread with two nuts in compression and used an impact drill to screw the anchors to maximum depth. We then performed vertical tensile pull tests until the screw anchors reached their capacity. We then extrapolated a relationship between the disk diameter and the maximum load capacity (shown in Figure 5.8). For the central core, we developed a 3" x 2" prototype, comprising of two $1\frac{1}{2}" \ x \ 2"$ box sections welded together and a pile-driving installation method to bury the section to competition depth. We then simulated a nacelle load by applying a lateral load, scaled up to competition specifications, and used that as our equivalent maximum reaction load.

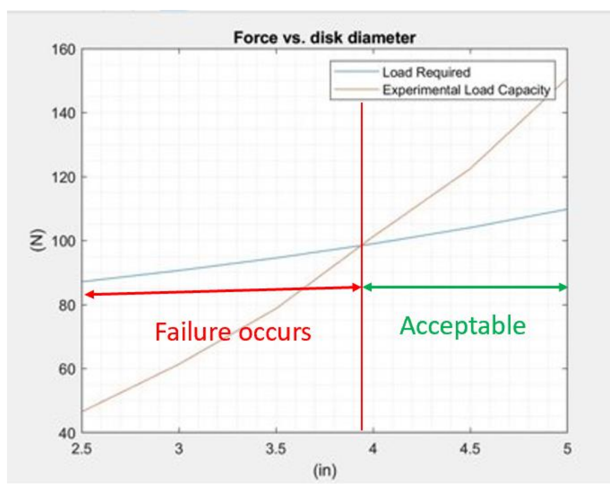

Figure 5.8 Helical Anchor Optimization

5.2.4 Analysis & Testing Synthesis

Our testing and analysis are synthesized in the following fashion: first, we developed static equilibrium equations using our force diagram (Figure 5.4) and the information provided in Section 5.2.2, used the lateral pull test from Section 5.2.3 on the hollow core to resolve the statically indeterminate equations, and the vertical pull tests on the screw anchors to develop a relationship between the load capacity and disk diameter. We superimposed the load required and the load capacity due to the changing disk diameter in Figure 5.8. It can be observed that the load capacity of the disk radius quickly outpaces the load required due to a changing disk diameter. Any disk diameter with a capacity that exceeds the required load is an acceptable disk diameter.

5.3 Manufacturing

The fabrication of the final foundation design relied primarily on CNC plasma cutting and TIG welding. The process started by converting the CAD model into 2D designs, then plasma cutting these parts. The scribe, the flat parts of the hollow core, and the helical anchors were plasma cut from varying thickness of sheet metal. The shell of the hollow core was made into two overlapping C shape sections from sheet using a press with a 90 degree insert. The initial steps manufacturing for the anchor legs was to cut the segments to the desired length on the vertical bandsaw. The transition piece and mid tube, which connects the hollow core to the scribe, were also cut to length on the bandsaw.

After all parts were rough cut, the slag was removed and the parts were prepared for welding. Prior to welding, the scribe was machined to accept the threaded weld nuts and allow for the passage of conductors. The scribe was then bent into shape, applying the desired anchor leg angle with respect to the vertical.

The welding phase of fabrication was split up into subcomponent groups: the helical anchors, the scribe, and the hollow core. The first step in fabricating the anchor legs was welding all thread and hollow tubing together. Afterwards, the disc was welded onto the end of the tubing. The scribe had its weld nuts tacked into place and verified for flushness before final welding. The transition piece was then affixed to the scribe with the assistance of a 3D printed jig. Using a jig yielded a more concentric and squarer finished product. The first step for the hollow core was to join the two sections of the core into a box section. The cap was then welded onto the box. The mid tube and adapter plate were joined, again using 3D printed jigs. Studs were then tacked into the adapter plate, allowing for the easy and precise connection to the scribe. The final step was to machine the holes into the hollow core for the conductors. The foundation was then assembled by threading the legs and bolting the hollow core into the scribe.

5.3.1 Foundation Testing

The foundation was installed into the substrate then tested by applying a lateral load at a set height on an attached testing tower (see Figure 5.9 for testing set-up). The moment created by this force was measured using a force gage. The force was increased until the tower reached the displacement limit, which was positioned 25mm in the direction of the force applied to mimic competition failure conditions. The tests were carried out at a smaller scale than competition load, so results had to be scaled up to meet competition standards. The testing height was 19.25 inches, whereas the full-scale height is expected to be 37 inches. To scale, our testing results yielded an average load capacity of 39.2 Newtons at competition height.

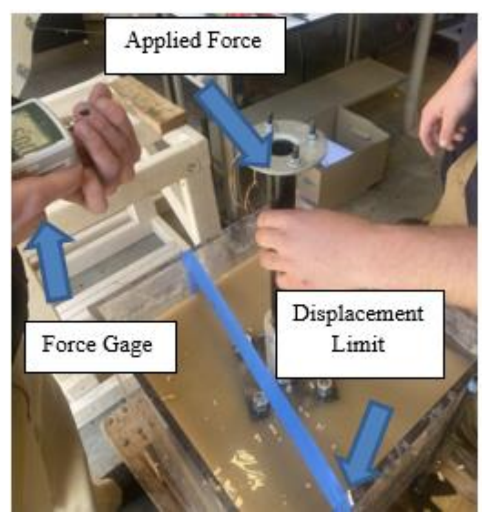

Figure 5.9: Foundation Test Set-Up

5.3.2 Goal Evaluation

Table II: Foundation Test Results

Trial #	Scribe to pull (in)	pull force (N)
1	19.25	75
2	19.25	75
3	19.25	70
4	19.25	81
5	19.25	76
Mean	19.25	75.4

The purpose of the foundation is to solidly anchor the wind turbine to the seabed, under all conditions. Through our initial analysis, we expect a peak loading condition of 14 N, applied at the nacelle. Using this as the benchmark, our full-scale testing showed a factor of safety of 2.8, with an average capacity 39.2 N. This test gave the team a high degree of confidence in our ability to meet the primary goal of stability.

This year, decreasing the weight of the foundation has been a priority in the design process. By utilizing new construction methods and an overhauled design philosophy, we were able to reduce the weight from 14.7 lbs to just 6.2 lbs, or a reduction of 58%, compared to last year's design.

5.4 Installation & Commissioning Checklist:

1) Inspect all components of foundation for wear or broken welds
2) Bolt hollow core section to scribe
3) Attach 4 anchors to scribe, with the anchors fully disengaged from the sand
4) Tighten driving nuts to anchor threads
5) Ensure sand surface is flat
6) Insert hollow core section to desired depth of 20 cm and check for level
7) Advance anchors into sand by hand until threads are fully engaged with scribe
8) When anchors are fully threaded into scribe, start advancement with impact gun
9) Begin screwing in anchors in staggered star pattern for even depth advancement
10) When anchors are halfway to desired depth, take smaller steps per drive
11) At full depth check level of foundation
12) Compress sand using required tool
13) Attach universal stub to scribe

Chapter 6: Power Electronics & Controls

6.1 Summary & Overview

The goal of the power electronics system is to maximize power production of the turbine while also safely rejecting its heat. In addition to the primary functionality of the electronics, the system must also meet safety functional requirements for emergency stop, and subsequent restart of the turbine system. Figure 6.1 is a simplified canonical diagram of power and controls electronics. The system was constructed in a manner similar to industrial process control boxes with components all mounted on DIN rails.

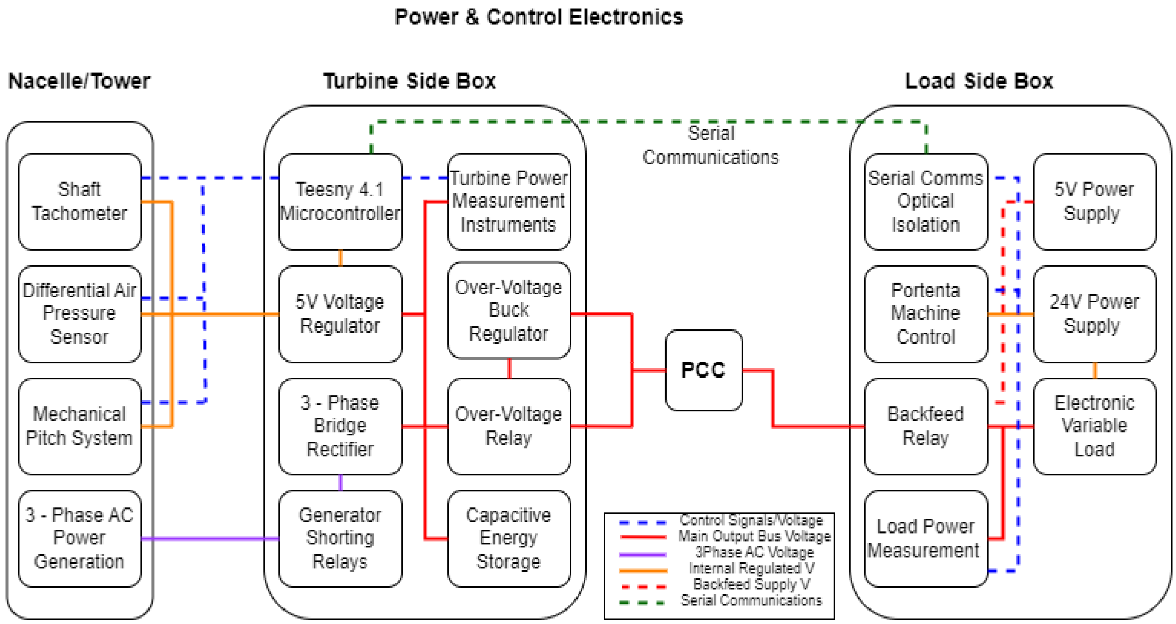

Figure 6.1: Electrical & Controls Canonical Diagram

6.2 Power Electronics

The primary changes from the 2022 Cal Maritime Power Electronics design include redundancy for emergency stop conditions, overvoltage protection, and optimized loading for rotor speed. A simplified one-line diagram of the electronics circuit can be found below in Figure 6.2.

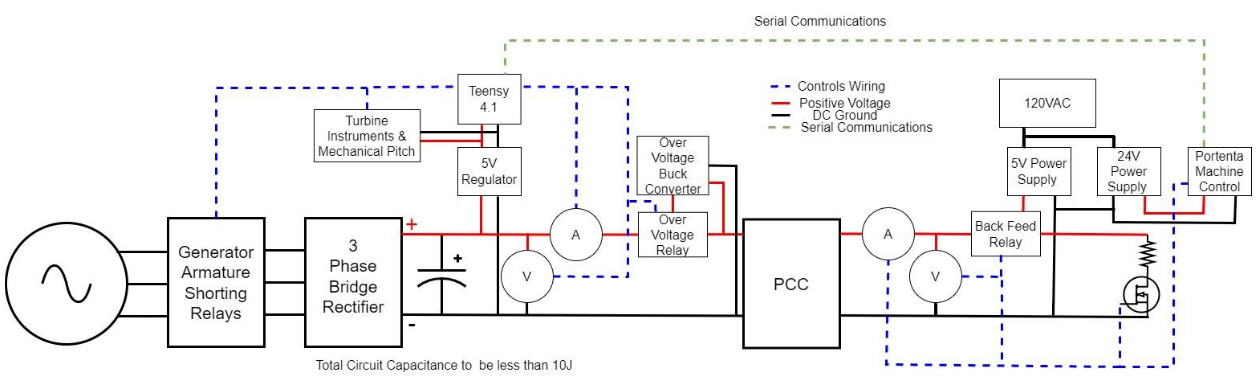

Figure 6.2: Simplified One-Line

The power electronics circuit first passes the three-phase power through two latching SPDT relays. These relays will be set to pass power through the bridge rectifier when the turbine is set to run and will be used to stop the rotor by shorting the three generator phases together for any turbine shutdown conditions. The rectified DC voltage produces approximately 9.8 joules of capacitive energy storage providing both power smoothing and power availability to allow the turbine pitch system to feather during the load disconnect case. The rectified DC voltage is also downregulated to 5VDC for the turbine control electronics. The system includes an overvoltage protection system which involves switching between a relay and a buck voltage regulator if the DC voltage rises past 44VDC. During normal operations, unregulated turbine voltage is passed to the load through the PCC. Two major changes from the 2022 Cal Maritime design are the addition of the relays used for shorting the turbine during an emergency stop and the overvoltage buck converter. The relays add redundancy for turbine emergency shutdown, and the buck converter solves the transient overvoltage condition seen during the 2022 competition.

The resistive load is the most significant change from the 2022 Cal Maritime Power Electronics. In the previous year, a constant resistive load was used, which does not require active control. This year, the load consists of a power resistor in series with an IRF530N N-Channel MOSFET.

The components put together serve as an analog voltage controlled current sink. The MOSFET controls the amount of current drawn by the load by changing the relative loading resistance of the circuit through the variation of the applied gate voltage. Shown in Figure 6.3 to the right is a plot of the experimental power curves for the Cal Maritime turbine this year. The two parabolic plots are two constant resistance power curves for the generator at 60 ohms and 30 ohms respectively. Where the resistance curve intersects the power curve is the power produced by the turbine at that wind speed. What is demonstrated by the 2 curves is that to maximize power at multiple wind speeds we need to be able adjust the loading resistance.

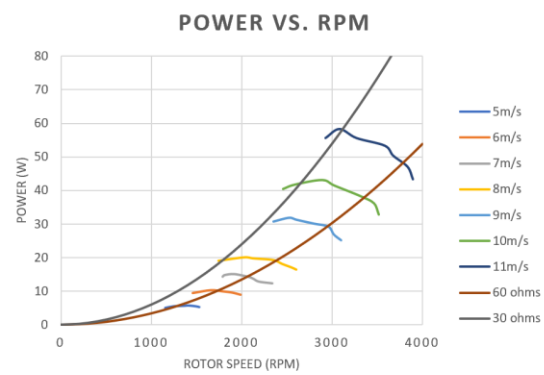

Figure 6.3: Power Curves for Turbine

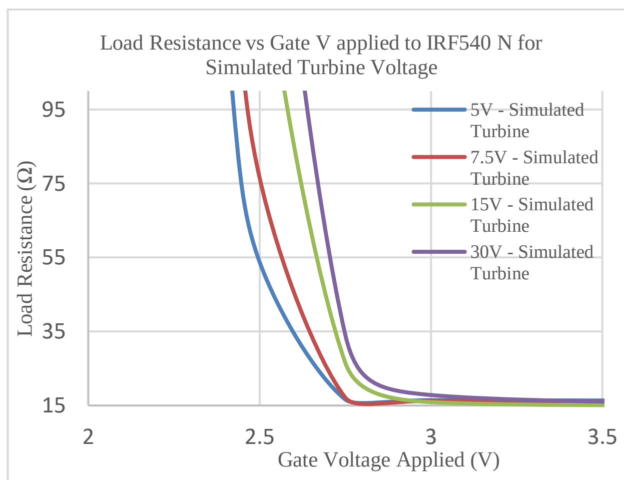

Figure 6.2: Controllable Loading Resistance Plot

The analog voltage to drive the MOSFET is provided to control the MOSFET from the Arduino Portenta Machine Control which is used to control the load electronics. The specifics of the control strategy can be found in the controls portion of this reportA. The MOSFET is cooled via a recycled CPU heatsink rated for 60W of heat dissipation. The variable loading allows us to maximize the power production of the turbine by ensuring that the loading on the generator keeps the rotor at its optimal speed for each wind speed. The load electronics are powered by 120VAC and regulated by a 24VDC and 5VDC power supply. The 24VDC is used to power the load microcontroller and the 5VDC Power supply is used to back feed power to the turbine electronics to restart the rotor after entering a turbine shutdown condition. Testing data shown in Figure 6.4 shows the controllable range of relative resistances up to a turbine voltage of 30V.

6.3 Controls Systems

The control system is responsible maximizing the effectiveness of the system while also maintaining the safety and durability of the system. The 2022 Cal Maritime control system can be characterized as a simple, yet effective system with only one control variable, blade pitch, and two points of instrumentation, current and voltage measurement. This year, we have implemented additional instrumentation to the turbine side controls with both a shaft tachometer and a pitot-tube for wind speed measurement, as well as the new electronic load discussed in the previous section.

6.3.1 Turbine Side Controls

The turbine control system is backboned on a Teensy 4.1 microcontroller. The controller was selected for its low power draw, high processing speed, IO, and it's built-in micro-SD card. The controller is responsible for processing data from the turbine instrumentation and uses a state-based software architecture to control the pitch system, braking, and overvoltage protection. The state diagram for the turbine side of the system can be found in the Figure 6.5 below. State 0 is the start up state, it sets the pitch of the blades to a less than optimal pitch angle to have the rotor cut in at a lower speed. As the rotor spins up and the Teensy microcontroller turns on, the controller will measure the shaft speed and power and transition the blade pitch to a full run status for State 1. When the system reaches rated power, the system will transition to State 2, which is when the controller will engage the pitch mechanism that modulates the rotor speed to ensure constant rotor speed after reaching 11m/s wind speed. Three possible conditions will bring the turbine into the shutdown condition: the E-Stop being actuated, the load being disconnected, and the wind speed exceeding 14m/s for the durability task. The E-Stop is a simple, normally closed switch, meaning that when the output goes low, the E-Stop has been actuated. The load disconnect will be triggered by a large drop in power production. The wind speed safety shutdown will be initiated by both the relative servo position of the blades and the wind speed measured by the pitot-tube.

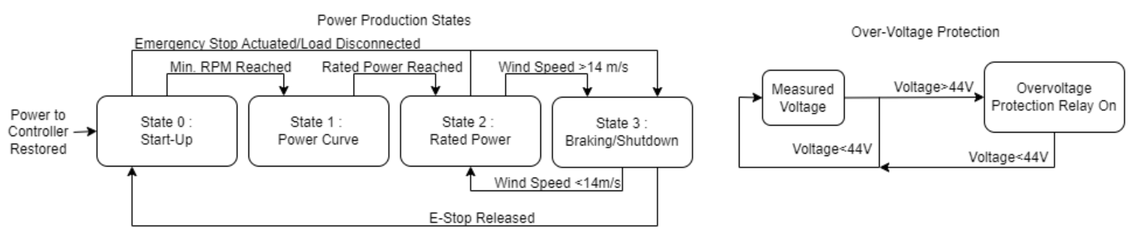

Figure 6.3: Turbine State Diagram

6.3.2 Load Side Controls

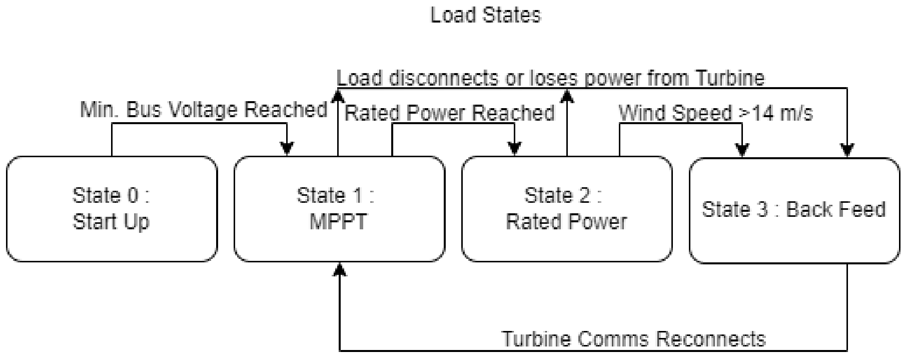

Figure 6.6 Load State Diagram

The load side controller is responsible for maximum power point tracking and supporting the restart of the turbine. A state diagram for the controller can be found in Figure 6.6. In state zero the load will set the gate voltage of the load electronics to zero and wait until the turbine is spinning effectively and the turbine controller is powered. The load will transition to state 1 which is a maximum power point tracking algorithm based on perturb and observe. The system will track to maximum power until the load reaches rated power. Once the load reaches rated power and transition to state 2 where the load will maintain a constant power output from the turbine. If the turbine shuts down and turbine communication's fails, the load will go to an open circuit on the MOSFET and begin back feeding 5VDC through to the Turbine through state 3.

Chapter 7: System Specifications

7.1 Turbine Testing

Our turbine field testing set-up consists of a wind tunnel that can run up to 14m/s. Additional instrumentation is installed to measure wind speed, voltage, current, and shaft speed. We tested for nameplate characteristics of our turbine to generate an experimental power curve and calculate annual energy production (AEP) to evaluate system-wide performance.

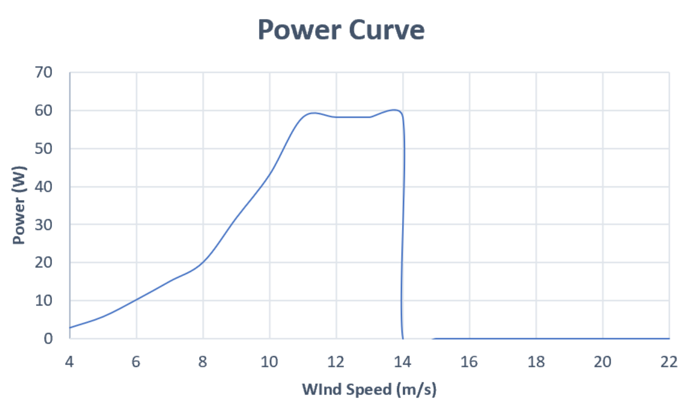

Figure 7.1: Turbine Power Curve

Shown in Figure 7.1 is our experimental power curve from start-up to the competition specified maximum wind speed of 22m/s. Power was maximized from 5-11m/s by manually varying a rheostat for optimal power with the slip rings and brushes installed. Beyond that, we have demonstrated that our pitch mechanism is able to shut down for the safety tasks and to cut-out at 14m/s for turbine durability. More work is being done for robust power and speed control for the pitch mechanism, and we are confident that it will be reliable before the competition.

Table III: Nameplate Turbine Characteristics

System Parameters	Values	Units
Rated Power	58.3	W
Rated Speed	3030	RPM
Operating Voltage	34.2	V
Start-up Wind Speed	4	m/s
Cut-out Wind Speed	14	m/s
AEP	41204	Wh
Turbine FS	2	N/A

Table III shows the nameplate characteristics of our system resulting from testing. The power is the highest measured we have seen in pre-competition (we expect minor parasitic losses since we will compete with our turbine electronics system), the operating speed is well-within our durable limits, the operating voltage is within a safe margin below the 48V limit, and we cut in at a low enough wind speed to power our controllers and actuators to run our turbine for maximum power. With an average wind speed of 3.8m/s in Vallejo, CA, we used a Rayleigh probability distribution to calculate wind speed probabilities throughout all ranges of wind speed. From the probability distribution, we calculated AEP for our turbine.

7.2 Commissioning Checklist

I. Mechanical Pitch System
   a. Using manual control software verify full range of pitching motion & ensure all fasteners are torqued appropriately.
   b. Verify Slip Ring continuity to servo & turbine side controller.

II. Generator
   a. Hand spin generator to check for 3-Phase power out put to the rectifier.
   b. Ensure condition of transmission cabling from Nacelle to Turbine Side electrical box is acceptable for safety and functionality.

III. Tower & Nacelle
   a. Adjust yaw of nacelle to prevailing wind direction, then appropriately torque

IV. Electronics & Controls
   a. Verify continuity between Turbine Electronics Output and Load Electronics Input
   b. Inspect and ensure that all external connections to electrical boxes have no signs of failure.
   c. Verify power supplies for load controller are correct voltage.
   d. Ensure heat rejection fans for load are running.
   e. Run wind tunnel to 5m/s – 14m/s
      i. Ensure that the instrumentation on the nacelle is functional.
      ii. Verify E-Stop state shuts down turbine
      iii. Verify load-disconnect shuts down turbine

In Memory of Evan Fishel
March 10th, 2001 – February 10th, 2023

Bibliography

[1] S. Farah, D. G. Anderson, and R. Langer, "Physical and mechanical properties of PLA, and their functions in widespread applications — A comprehensive review," *Advanced Drug Delivery Reviews*, vol. 107, no. 0169-409X, pp. 367–392, Dec. 2016, doi: https://doi.org/10.1016/j.addr.2016.06.012.

[2] T. Brown *et al.*, "U.S. Department of Energy Collegiate Wind Competition: Technical Design Report 2020," California State University Maritime Academy, 2020.

[3] "spl10b.pdf | Unified Engineering I, II, III, & IV | Aeronautics and Astronautics," *MIT OpenCourseWare*. https://ocw.mit.edu/courses/16-01-unified-engineering-i-ii-iii-iv-fall-2005-spring-2006/resources/spl10b/

[4] R. G. Budynas, *Roark's Formulas For Stress And Strain.* S.L.: Mcgraw-Hill Education, 2020.

[5] K. Shin *et al.*, "U.S Department of Energy Collegiate Wind Competition:Technical Design Report 2022," California State University Maritime Academy, 2022.

[6] H. Electric Motors, "bavaria-direct.co.za," *www.bavaria-direct.co.za*. https://www.bavaria-direct.co.za/scheme/calculator/ (accessed May 04, 2023).

[7] K. Magnetics, "Halbach Arrays," *Kjmagnetics.com*, 2020. https://www.kjmagnetics.com/blog.asp?p=halbach-arrays

[8] Fixed Offshore Foundation Types . (n.d.). tethys.pnnl.gov. Retrieved May 3, 2023, from https://tethys.pnnl.gov/technology/fixed-offshore-wind.